Available online at www.sciencedirect.com

ScienceDirect

journal homepage: www.elsevier.com/locate/he

Hydrogen production by methane pyrolysis in molten binary copper alloys

David Scheiblehner[*], *David Neuschitzer*, *Stefan Wibner*, *Andreas Sprung*, *Helmut Antrekowitsch*

Nonferrous Metallurgy, Montanuniversitaet Leoben, Leoben, 8700, Austria

HIGHLIGHTS

- CH_4 conversion rates are strongly influenced by the choice of metal or alloy.
- CuNi alloys show high catalytic activities in the pyrolysis of methane.
- The low surface tensions of, e.g., CuBi alloys are beneficial for the reaction yield of methane pyrolysis.
- The morphology and purity of produced carbons can be modified by varying process parameters.

GRAPHICAL ABSTRACT

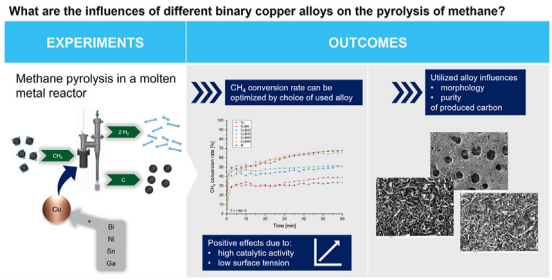

ARTICLE INFO

Article history:
Received 7 June 2022
Received in revised form
1 August 2022
Accepted 11 August 2022
Available online 2 September 2022

Keywords:
Hydrogen production
Carbon production
Methane Pyrolysis
Molten metal catalysts
Surface tension
Copper alloys

ABSTRACT

The utilization of hydrogen as an energy carrier and reduction agent in important industrial sectors is considered a key parameter on the way to a sustainable future. Steam reforming of methane is currently the most industrially used process to produce hydrogen. One major drawback of this method is the simultaneous generation of carbon dioxide. Methane pyrolysis represents a viable alternative as the basic reaction produces no CO_2 but solid carbon besides hydrogen. The aim of this study is the investigation of different molten copper alloys regarding their efficiency as catalytic media for the pyrolysis of methane in an inductively heated bubble column reactor. The conducted experiments demonstrate a strong influence of the catalyst in use on the one hand on the conversion rate of methane and on the other hand on the properties of the produced carbon. Optimization of these parameters is of crucial importance to achieve the economic competitiveness of the process.

Abbreviations: CCUS, carbon capture, utilization, and storage; PAHs, polyaromatic hydrocarbons.

* *Corresponding author.*
E-mail address: david.scheiblehner@unileoben.ac.at (D. Scheiblehner).

https://doi.org/10.1016/j.ijhydene.2022.08.115

Introduction

At present approximately 80% of the total world energy supply depends on the use of fossil hydrocarbons such as coal or oil. Global CO_2 emissions mainly occurring in industrial processes and due to the combustion of fossil fuels or non-renewable wastes amounted to 34,156 Mt in 2020. A transition of the energy supply system based on these traditional resources to achieve the goal of CO_2-neutrality including the primary purpose of mitigating the anthropogenic greenhouse effect is – despite all ideological and political controversies – one of the most urgent challenges of the 21st century [1–3].

The fields of research and development of processes applied for the production and utilization of hydrogen to facilitate substitution of conventional energy carriers and reducing agents, especially in important industrial sectors such as transport, metallurgy, or energy technology, as well as the investigation and improvement of methods that ensure short and long term reliability and affordability of H_2 storage and infrastructure are considered critical key variables on the way towards a sustainable future [2,4–8].

One-fifth of the hydrogen produced globally is occurring as a by-product, mainly in refineries during the reformation of naphtha into gasoline. The remaining part is generated almost entirely from fossil fuels, whereas natural gas is followed by coal as the most important feedstocks. The percentage of hydrogen which comes from the electrolysis of water currently occupies a negligible proportion. The dominant position of fossil fuels as raw materials for hydrogen production is reflected in the balance of CO_2 emissions caused by energy and industrial sectors globally. In 2020, approximately 900 Mt of direct CO_2 emissions originating from H_2 production were recorded. This value is equivalent to the cumulative emissions of Indonesia and the United Kingdom and shows that the development of CO_2-neutral processes in these areas must occupy an essential position in the future. Fig. 1 compares the sources of the 2020 global hydrogen production [8].

The most commonly used technology for the industrial production of hydrogen is steam reforming of hydrocarbons, methane in particular. The endothermic process is operated

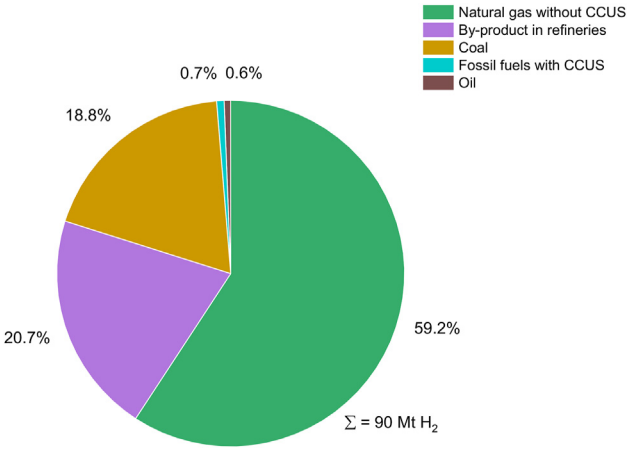

Fig. 1 – Feedstock for the production of hydrogen (2020) [8].

at an elevated pressure at 970–1100 K in the presence of a catalyst (mostly nickel). The overall reaction can be described as a combination of the actual reforming reaction (see Equation (1)) and the water-gas-shift reaction (see Equation (2)) [9–11].

$$CH_4 + H_2O \rightarrow CO + 3\,H_2, \Delta H_R^0 = 206\,\frac{kJ}{mol} \quad (1)$$

$$CO + H_2O \rightarrow CO_2 + H_2, \Delta H_R^0 = -41\,\frac{kJ}{mol} \quad (2)$$

The overall reaction is given in Equation (3): [9,10].

$$CH_4 + 2\,H_2O \rightarrow CO_2 + 4\,H_2, \Delta H_R^0 = 165\,\frac{kJ}{mol} \quad (3)$$

To produce one mol of hydrogen in this reaction the energy of 41 kJ must be provided. The generation of high-purity hydrogen (99.99 vol%) requires its separation from the remaining gas stream. This process step is usually realized by pressure swing adsorption. Steam reforming of methane is considered a sophisticated technology with high production rates and good economic efficiency. The product costs are primarily determined by the price of natural gas. One main disadvantage is the production of CO_2 that is associated with this technology [9,10,12,13].

Especially concerning carbon sequestration, the electrolysis of water represents a promising alternative to traditional methods for the production of hydrogen. The utilization of electrical energy allows a decomposition of the source material water into high-purity hydrogen and oxygen according to Equation (4) [9,13].

$$H_2O \leftrightarrow H_2 + 0.5\,O_2; \Delta H_R^0 = 286\,\frac{kJ}{mol} \quad (4)$$

The economics and ecology of this technology directly depend on the price and carbon footprint of the electrical energy source. In this respect, electrolysis is particularly suitable for decentralized applications. Currently, most of the required energy originates from fossil fuels, which is adversely impacting the carbon footprint and the comparatively high energy requirement is one of the biggest disadvantages of the process. However, if 100% of the used electricity can be provided by regenerative energy sources, water electrolysis offers the sole completely CO_2-neutral option for hydrogen production to date [9,13,14].

Methane pyrolysis describes the one-step process of thermal cracking of methane in presence of a catalyst to form hydrogen and carbon according to Equation 5 [9,13].

$$CH_4 \leftrightarrow C + 2\,H_2; \Delta H_R^0 = 76\,\frac{kJ}{mol} \quad (5)$$

The required heat of 38 kJ/mol H_2 can be provided electrically or by combustion of fossil fuels. Transition metals such as iron, nickel, or cobalt, activated carbon, or metal oxides in solid form are frequently used as catalysts. The rapid deactivation of these catalysts due to the produced carbon has a highly detrimental effect on the overall efficiency. Several innovations including the utilization of molten catalytic alloys on which the hardly soluble pyrolysis carbon floats bear the potential to remedy this disadvantage. The

economics of the process primarily depends on the cost of natural gas, but the marketability and price of the pyrolysis carbon produced could represent further significant factors in the future. Considering the potential of variable CO_2 charges as well as technological advancements that may improve the process efficiency methane pyrolysis is regarded as an ecologically promising, cost-effective bridging technology [9,12,13,15–17].

Investigations of the effectiveness of different metals and alloys as well as reactor or gas injection concepts for methane pyrolysis have been the subject of research for several years. Serban, Lewis et al. [18] performed experiments in a reactor filled with low-melting metals (lead or tin), solid materials (SiC or Al_2O_3), or a mixture thereof. They demonstrated that the use of porous gas introduction systems entails a significant increase in efficiency compared to single pipes. In experiments with liquid tin Plevan, Geißler et al. [19] measured a strong influence of the flow rate of methane. An increase in this parameter is associated with a significant decrease in CH_4 conversion, whereas an increase in temperature has a positive effect on the hydrogen yield. Geißler, Abánades et al. [20] performed experiments in a 1 m liquid metal bubble column reactor fitted with a liquid tin packed bed inventory. The highest CH_4 conversion rate measured was 78% at 1175 °C and 50 ml_n/min, with gas injection via a single nozzle in the bottom ($\varnothing = 0.5$ mm). Upham, Agarwal et al. [21] worked with a 1.1 m bubble column reactor in combination with a molten 27 at% Ni/73 at% Bi alloy. At a temperature of 1065 °C, a CH_4 conversion of 95% was achieved. With the same alloy previously used by Upham, Agarwal et al. [21] and an additional layer of sodium bromide, Rahimi, Kang et al. [22] were able to achieve a methane conversion of 37.5% in a 1 m bubble column reactor at 1000 °C. In this research, pure methane was introduced through a quartz tube ($d_i = 2$ mm; $d_o = 3$ mm) at a flow rate of 10 ml_n/min. An additional salt layer had a positive effect on the purity of the produced carbon and its metal contamination decreased with increasing layer height. Palmer, Tarazkar et al. [23] conducted experiments with Cu–Bi melts. They demonstrated a correlation between the effectiveness of the alloys used and their surface tension. At temperatures up to 976.85 °C and a residence time of about 12 s, it was possible to measure a methane conversion of more than 30% in a bubble column reactor with liquid tellurium in experiments by Zeng, Tarazkar et al. [24]. They showed that the catalytic effect of gaseous tellurium is lower than that of liquid tellurium. However, an industrial application is not likely in the foreseeable future due to the rarity, high price, and volatility of the metal used. Leal Pérez, Jiménez et al. [25] were able to increase CH_4 conversion rates up to 91% at 1119 °C by using a gallium melt in a bubble column reactor where the introduction of a 50 vol% Ar/50 vol% CH_4 mixture was realized utilizing porous plate distributors made of quartz at a flow rate of 450 ml_n/min. Zaghloul, Kodama et al. [26] demonstrated the effect of adding different, catalytically active metals (copper or nickel) to the base metal tin in a bubble column reactor. The presence of Cu or Ni led to an increased hydrogen yield. With an alloy consisting of 95 wt% Sn and 5 wt% Cu, a CH_4 conversion of 19% at 1050 °C was achieved when a gas mixture of methane diluted by nitrogen to 65 vol% was fed through a quartz tube from above at a flow rate of 70 ml_n/min [18–26].

The dominant aggregate in research on the topic of methane pyrolysis with molten metal catalysts is the bubble column reactor which essentially consists of a cylindrical vessel with a length to diameter ratio of more than five, that is at least partially filled with a liquid phase or a suspension and mostly heated electrically. Gases can be introduced in the lower part of the reactor by various systems. Advantages of this type of multiphase reactor include excellent heat and mass transfer coefficients and low maintenance and operating costs [27,28].

Classification according to the prevailing flow regime that develops depending, inter alia, on superficial gas velocity and column diameter can be made. Three main flow regimes can be identified: the bubbly flow (homogenous) regime which occurs at low superficial velocities and is characterized by gentle mixing and practically no coalescence or breaking-up of the bubbles thus resulting in a relatively uniform bubble size distribution, the churn-turbulent (heterogenous) regime at higher superficial velocities, where turbulent mixing, bubble coalescence and breaking up and therefore a wider range of bubble size can be found and the slug flow regime which has only been observed at a laboratory scale in columns with small diameters at high superficial velocities [28–30].

In general, the formation of small bubbles is desirable to create a large gas-liquid interfacial area which positively impacts mass transfer rates [31,32]. Using the volume-of-fluid method to simulate the formation and motion of a single bubble in liquids with varying properties Zahedi, Saleh et al. [33] demonstrated that increasing surface tensions result in longer bubble detachment times from the orifice. If a greater amount of gas can stream into the bubble, the average bubble diameter increases. Furthermore, higher liquid densities shifted the bubble diameters to smaller values, whereas changes in liquid viscosity have an insignificant effect. These correlations can also be found in a series of empirical formulas valid for bubble formation at single nozzles in different melts as developed e.g., by Tate [34], Mori, Sano et al. [35], and Sano and Mori [36]. [31–36].

The aim of this work is a comparison of different binary copper alloys according to their effectiveness as catalytic media in methane pyrolysis, further enabling lower process temperatures while maintaining constant methane conversion rates, thus optimizing the process in terms of energy consumption. For this purpose, various experiments were carried out in an inductively heated bubble column reactor, while keeping metal volume, process temperature and methane volume flow constant. These constraints allow an isolated investigation of the influence of different alloys and their physical and chemical properties. A comparison of the results with calculated values for surface tension and liquid density aims to advance the further improvement of the catalytic melts in use.

Materials and methods

A schematic representation of the experimental reactor is shown in Fig. 2. The catalytic metals or alloys are melted in a graphite crucible with an inner diameter of 6.5 cm by induction heating. The process temperature is determined with two

thermocouples (type K) located outside the bottom of the crucible and logged continuously during the experiment. A graphite flange connects the crucible with an airtight stainless steel piping system. Methane (purity ≥99.5 vol%) is introduced into the liquid catalyst through a lance made of Al_2O_3 (purity >99.5 wt%). Product gas flows along the welded or bolted tubes and exits the experimental setup via a hot gas filter (Pall Dia-Schumalith® DS 03–20 filter element; $d_o = 50$ mm, $d_i = 20$ mm, $l = 135$ mm) while the gas composition is measured simultaneously in a gas analyzer (ABB EL 3020 with Uras26 infrared photometer and Caldos27 thermal conductivity analyzer). The produced carbon either floats on the surface of the bath or is entrained in the gas flow, separated from the gaseous stream by the hot gas filter, and collected in a glass bottle. Previous experiments demonstrated the formation of intermediates, mainly polyaromatic hydrocarbons, besides hydrogen in the process. To avoid condensation of these PAHs in the hot gas filter, the corresponding section of the piping system is heated to a temperature of 300 °C by heating wires. Additional flushing with nitrogen (purity ≥99.8 vol%) which is introduced into the system employing a stainless-steel lance results in a higher gas flow rate in the system to avoid an accumulation of solid particles, especially in the horizontal pipe section.

To prepare the catalytic alloys, copper chips, bismuth pellets, nickel powder, tin ingots, and gallium shots with minimum purities of 99.90 wt%, 99.99 wt%, 99.995 wt%, 99.99 wt%, and 99.99 wt%, respectively, were used. A calculation of the mass which corresponds with a constant level of the melt of 7 cm for each catalyst was performed. The temperature-dependent densities of the investigated binary alloys were therefore computed by linear approximation between the quantities of the pure metals at process temperature. The required data were obtained from Smithells metals reference book [37]. As methane should be introduced into a liquid catalyst the liquidus temperature of each metal or alloy respectively was computed using FactSage 8.0 and the process temperature is adjusted accordingly. The investigated catalytic metals and alloys as well as their mentioned properties are listed in Table 1. The notation of the alloys gives the amount of the alloying element in at% that is added to the base metal copper. As CuNi12.5 has the highest liquidus temperature of 1156.16 °C for each experiment 1160 °C and 1 atm ab were selected as process temperature and pressure, respectively.

The required mass of each metal is weighed in and molten in the graphite crucible before the piping system is closed and the experimental setup is flushed with nitrogen. Ensuring the system's airtightness is performed through a manometer at the gas outlet. At this stage, the Al_2O_3 lance is

Table 1 – Investigated metals/alloys (element contents in at%) as well as their corresponding densities at 1160 °C (linear approximation for alloys) and liquidus temperatures computed using FactSage 8.0

Metal/Alloy	Density [kg/m^3]	Liquidus temperature [°C]
Cu	7938.28	1084.62
Bi	9000.80	271.40
Sn	6413.83	231.93
CuBi5	8095.05	1033.62
CuBi20	8417.69	940.81
CuBi40	8667.98	874.73
CuBi60	8821.71	803.42
CuBi80	8925.74	694.10
CuSn20	7452.97	791.36
CuSn40	7092.75	654.20
CuSn60	6814.77	546.51
CuSn80	6593.76	466.33
CuNi2.5	7945.60	1099.85
CuNi5	7952.95	1114.58
CuNi7.5	7960.32	1128.85
CuNi10	7967.73	1142.71
CuNi12.5	7975.16	1156.16
CuGa2.5	7870.66	1073.16
CuGa5	7803.36	1058.8
CuGa7.5	7736.39	1041.77
CuGa10	7669.74	1022.17

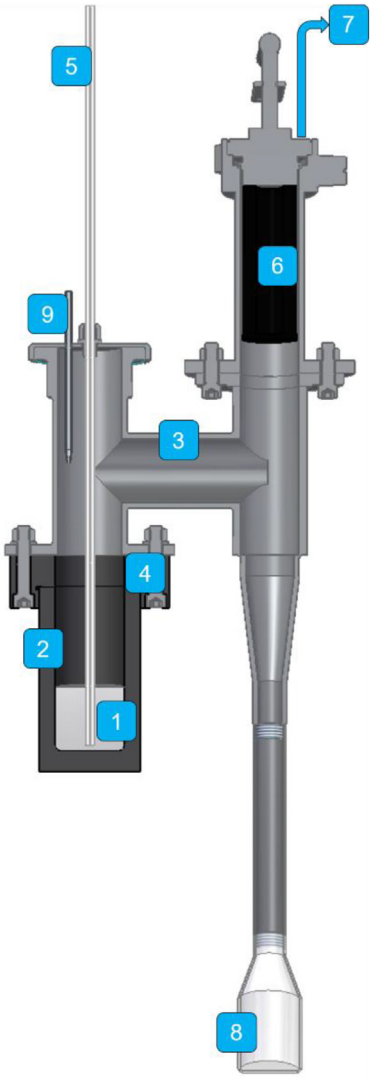

Fig. 2 – Schematic representation of the research reactor. (1) Molten metal catalyst, (2) graphite crucible, (3) piping system, (4) graphite flange, (5) Al_2O_3 lance (CH_4-supply), (6) hot gas filter, (7) gas analyzer, (8) glass bottle, (9) stainless steel lance (N_2-supply).

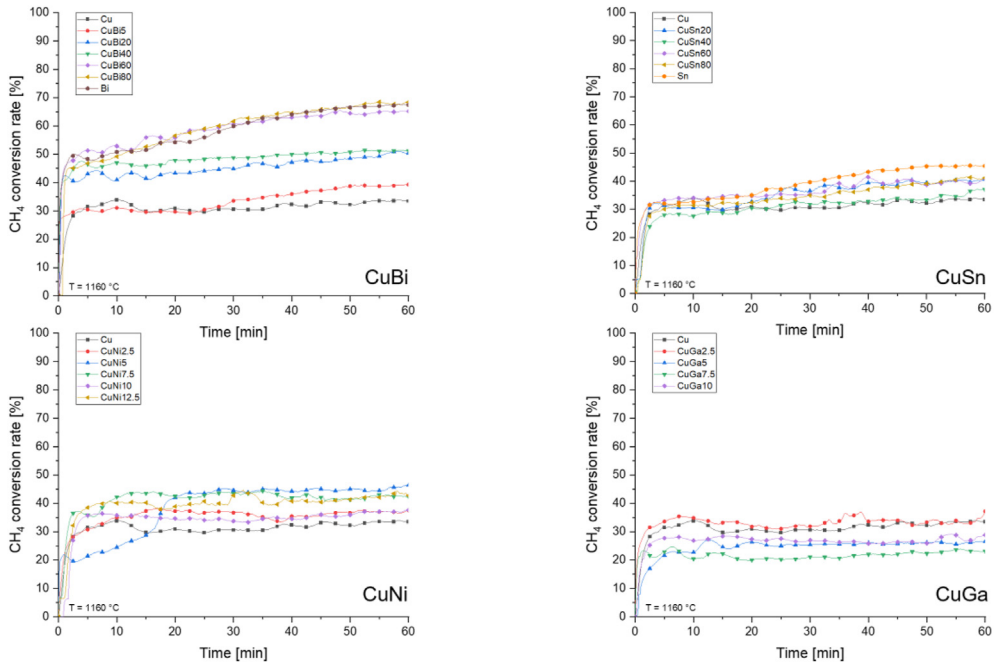

Fig. 3 – Methane conversion rates for different investigated binary copper alloys over experimental time at a process temperature of 1160 °C and a CH_4 flow rate of 500 ml_n/min.

positioned above the metal. Once airtightness is guaranteed and process temperature is reached methane is introduced into the system at a flow rate of 500 ml_n/min (controlled with Bronkhorst digital flow meters), and the alumina lance is lowered into the melt until the distance to the inner bottom of the crucible has decreased to 0.5 cm and the analysis of the produced gas stream is started. Concerning bubble diameter, bubble distribution in the melt, and the resulting reactive surface, the utilization of a lance has disadvantages compared to other systems for the introduction of gas for example impeller or flushing stones. However, gas injection via lances was chosen for these experiments, as the construction is simple, and the system is insensitive to changes in process parameters and catalysts.

Results

During the experiments, the hydrogen content in the product gas is measured continuously in the gas analyzer. The recorded content of CH_4 in the produced gas stream, X_{CH4}, as well as the adjusted volumetric input flow rates of CH_4 and N_2, V_{CH4}, and V_{N2}, are used to calculate the corresponding amount of dissociated CH_4 according to the stoichiometry of Equation (5) and further the consequential methane conversion rates (cf. Equation (6)). Fig. 3 depicts the results of these calculations as functions of the experimental time for the investigated metals and alloys (cf. Table 1). Table 2 lists the determined values at specific time increments.

$$CH_4\ conversion\ rate = \frac{\dot{V}_{CH_4} \cdot (100 - X_{CH_4}) - \dot{V}_{N_2} \cdot X_{CH_4}}{\dot{V}_{CH_4} \cdot \left(1 + \frac{X_{CH_4}}{100}\right)} \quad (6)$$

In most experiments, improved results can be recorded as the experiments are running longer. For CuBi and CuSn alloys tendencies to higher conversion rates can be found as the content of the alloying element is increased. Overall CuBi alloys show the best efficiency followed by CuNi, CuSn, and CuGa alloys. The highest methane conversion rate of

Table 2 – CH_4-conversion determined at time steps of 10 min.

Metal/Alloy	CH_4-conversion [%] after t [min]					
	t = 10	t = 20	t = 30	t = 40	t = 50	t = 60
Cu	33.84	30.86	30.58	32.33	32.19	33.46
Bi	50.78	54.22	59.93	64.06	66.52	67.42
Sn	32.58	35.02	39.68	43.28	45.29	45.39
CuBi5	31.03	29.69	33.56	35.97	38.73	39.29
CuBi20	40.99	43.31	44.87	47.20	48.51	50.41
CuBi40	46.98	47.83	48.78	49.94	50.73	51.31
CuBi60	52.86	55.89	60.60	63.02	64.45	65.16
CuBi80	49.18	56.57	61.60	64.48	66.37	68.44
CuSn20	30.55	32.75	36.56	39.41	39.45	40.70
CuSn40	27.55	30.44	31.81	32.78	33.29	37.07
CuSn60	34,03	34,68	35,36	41,46	38,72	41,02
CuSn80	31.45	32.40	34.96	37.01	39.12	41.18
CuNi2.5	34.99	37.26	36.71	35.46	36.64	37.49
CuNi5	44.10	46.80	46.16	45.98	44.95	55.75
CuNi7.5	42.27	42.47	43.49	41.84	41.26	42.43
CuNi10	35.81	34.65	33.72	34.52	35.95	37.70
CuNi12.5	40.08	38.87	42.78	40.73	41.34	42.74
CuGa2.5	34.83	31.74	31.87	33.62	33.37	37.22
CuGa5	22.73	26.34	25.44	26.08	26.19	26.50
CuGa7.5	31.59	27.44	26.73	30.06	30.59	35.95
CuGa10	26.90	27.38	26.99	25.86	25.93	28.86

approximately 68% could be calculated for experiments with CuBi80 and pure Bi at 60 min.

Additionally, the produced carbon is analyzed in a JEOL JSMIT300 scanning electron microscope with energy-dispersive X-ray spectroscopy. Fig. 4 depicts SEM/BSE images of carbon deposited in the hot gas filter at different experiments. In experiments with CuBi and CuGa alloys, the produced solid fraction consists of very fine granular agglomerates. The use of CuSn and CuNi alloys results in a loose and fibrous structure. As the Sn amount increases, the individual particles gain in size.

The results of the SEM/EDS analysis are listed in Table 3. The lowest carbon content of 94.29 and 96.71 at% respectively can be found in the samples originating from experiments with CuBi40 and CuBi80 whereas the purest carbon originates from experiments with CuSn80 and CuGa5 with a carbon content of 99.87 and 99.90 at% respectively.

Calculations

The superficial gas velocity, u_s, is calculated as a relation of volumetric flow rate, V, to the cross-sectional area of the column, A_c, (cf. Equation (7)) which results in 2.511 E−03 m/s for the experiments of this work.

$$u_s = \frac{\dot{V}}{A_c} \tag{7}$$

A fundamental correlation between bulk phase and surface phase composition and surface tension of the investigated alloys is given by Butler [38] (cf. Equation (8)).

$$\sigma = \sigma_i + \frac{RT}{A_i} ln \frac{N_i^S}{N_i^B} + \frac{1}{A_i}\left[G_i^{E,\,S}\left(T,\,N_i^S\right) - G_i^{E,\,B}\left(T,\,N_i^B\right)\right] \tag{8}$$

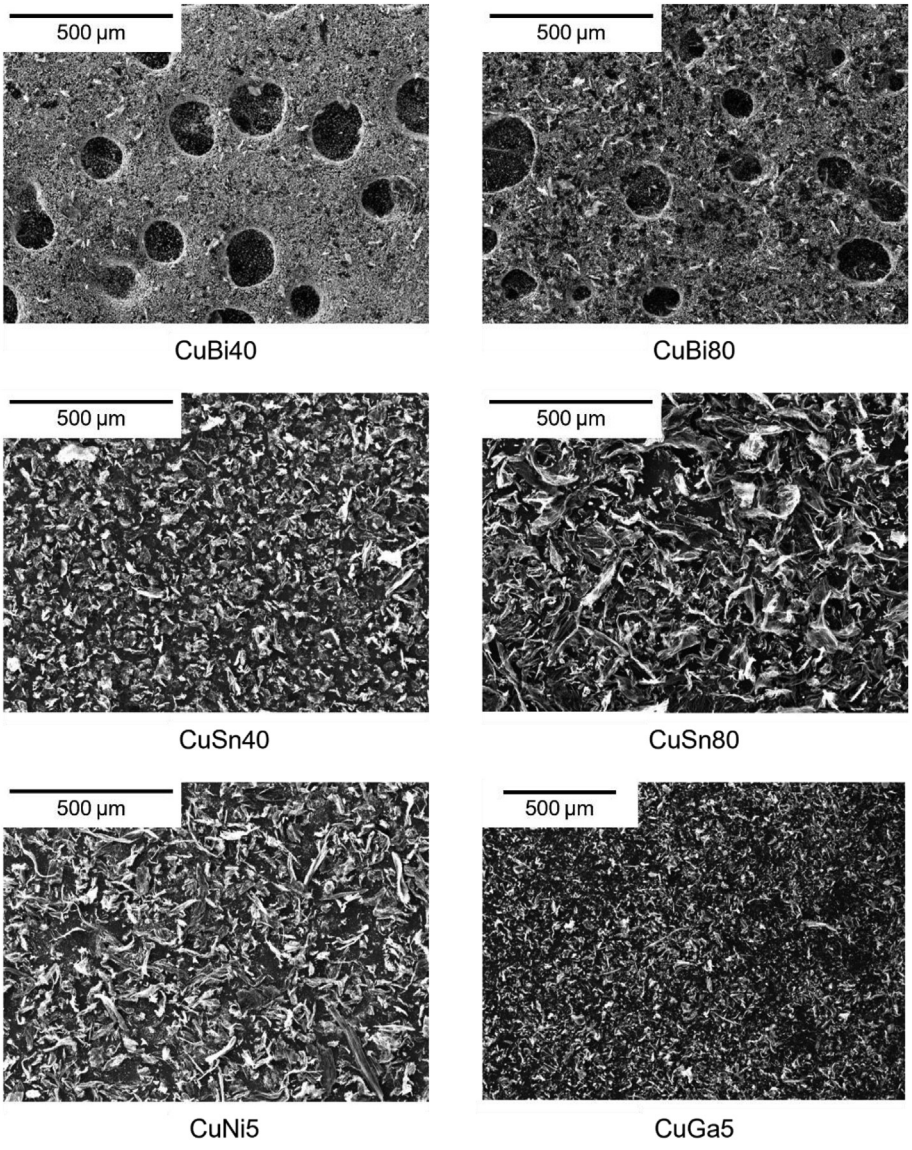

Fig. 4 – SEM/BSE images of the carbon fractions of experiments with the alloys CuBi40, CuBi80, CuSn40, CuSn80, CuNi5 and CuGa5.

Table 3 – SEM/EDS analysis of carbon from experiments carried out using different alloys.

Alloy	Element content [at%]					
	C	Cu	Bi	Sn	Ni	Ga
CuBi40	94.29	0.39	5.32	0	0	0
CuBi80	96.71	0.19	3.10	0	0	0
CuSn40	99.38	0.38	0	0.24	0	0
CuSn80	99.87	0.11	0	0.02	0	0
CuNi5	99.67	0.33	0	0	0	0
CuGa5	99.90	0.05	0	0	0	0.05

In Equation (8), superscripts S and B identify surface phase and bulk phase, respectively, σ_i describes the surface tension of the pure metal i, R the molar gas constant, T the temperature, A_i the molar surface area of component i, N_i^{sup} the mole fraction of metal i in surface phase (sup = S) or bulk phase (sup = B) and $G_i^{E,\ sup}$ the partial excess Gibbs energy of component i in surface phase (sup = S) or bulk phase (sup = B). A_i is calculated according to Equation (9), with N_0, the Avogadro's number, L, a geometric factor (L = 1.091 for liquid metals), and V_i, the molar volume of pure metal i. In Equations (8) and (9) the required values of surface tension, density, and molar mass of pure metals are given by Smithells metals reference book [37].

$$A_i = L \cdot N_0^{1/3} \cdot V_i^{2/3} \tag{9}$$

Thermodynamic data used to calculate Redlich-Kister polynomials to approximate the partial excess Gibbs energies were obtained from Mey [39], Niemelä, Effenberg et al. [40], Li, Franke et al. [41] and Li, Ji et al. [42]. The partial excess Gibbs energy of component i in the surface phase can be estimated using an approximation given by Speiser, Poirier et al. [43] (cf. Equation (10)).

$$G_i^{E,\ S} = \beta \cdot G_i^{E,\ B} \tag{10}$$

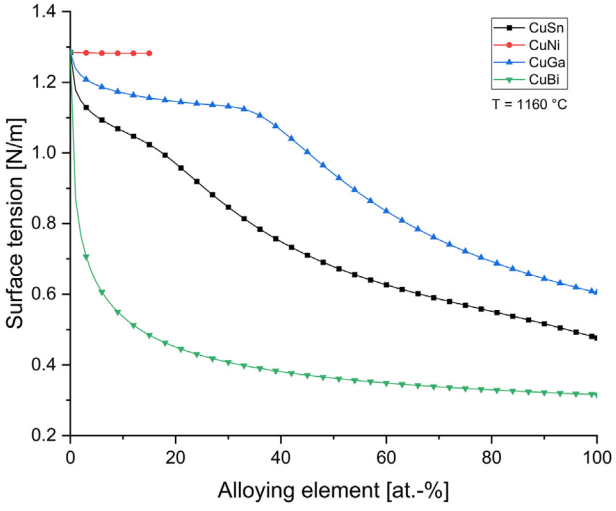

Fig. 5 – Surface tensions of the investigated liquid alloys as calculated using Butler Equation as functions of the alloying element contents (cf. Equation (8)).

In Equation (10) the parameter β gives the ratio of the coordination number Z in the surface phase to that in the bulk phase. In this work, a value of 0.83 is chosen for β as given by Tanaka, Hack et al. [44] for liquid metals.

After inserting all known values for surface tension and molar surface areas of the pure metals, as well as partial excess Gibbs energies in Equation (8), surface tension and composition of the surface phase of the investigated alloy are determined numerically by implementing an evolutionary algorithm. Fig. 5 depicts the resulting values for the surface tension of the investigated binary Cu-alloys at 1160 °C as a function of the alloying elements' content. The surface tension of pure copper at 1160 °C is 1.285 N/m. The addition of Ni, Ga, Sn, or Bi leads to a more or less strong decrease in surface tension. Overall, CuNi alloys have the highest surface tension, followed by CuGa and CuSn alloys. The surface tension of CuBi alloys is the lowest of the investigated systems. CuNi alloys were investigated in the range of 0.0–15 at% Ni as liquidus temperature exceeds process temperature of 1160 °C at higher Ni contents. In this range, the addition of nickel to pure copper shows no significant effect. An addition of Ga shifts the surface tension to lower values. The gradient of this curve decreases until the value of 33 at% of Ga is reached and rises again at a further increase of the gallium content. At 100% Ga, the surface tension of 0.605 N/m can be calculated at 1160 °C. Gradually adding tin to a melt of 100 at% Cu leads to decreasing surface tension. The gradient of the corresponding diagram shows only slight variations. For pure tin, the surface tension of 0.476 N/m is determined. Even small additions of bismuth lead to a sharp decline in the curve. A melt of pure bismuth has the lowest surface tension in this work with 0.316 N/m at the given temperature. The calculated surface tensions of the investigated alloys at 1160 °C are listed in Table 4.

Mori, Sano et al. [35] proposed a correlation between surface tension, liquid density, gas flow rate, and the size of

Table 4 – Calculated surface tensions and bubble diameters of the investigated alloys at 1160 °C.

Metal/Alloy	σ [N/m]	d_b [mm]
Cu	1.285	10.596
Bi	0.316	9.670
Sn	0.476	9.862
CuBi5	0.632	9.887
CuBi20	0.450	9.745
CuBi40	0.381	9.702
CuBi60	0.349	9.685
CuBi80	0.329	9.676
CuSn20	0,970	10.299
CuSn40	0.749	10.089
CuSn60	0.627	9.984
CuSn80	0.552	9.925
CuNi2.5	1.284	10.594
CuNi5	1.283	10.591
CuNi7.5	1.283	10.589
CuNi10	1.282	10.587
CuNi12.5	1.282	10.585
CuGa2.5	1.214	10.522
CuGa5	1.193	10.509
CuGa7.5	1.180	10.506
CuGa10	1.170	10.507

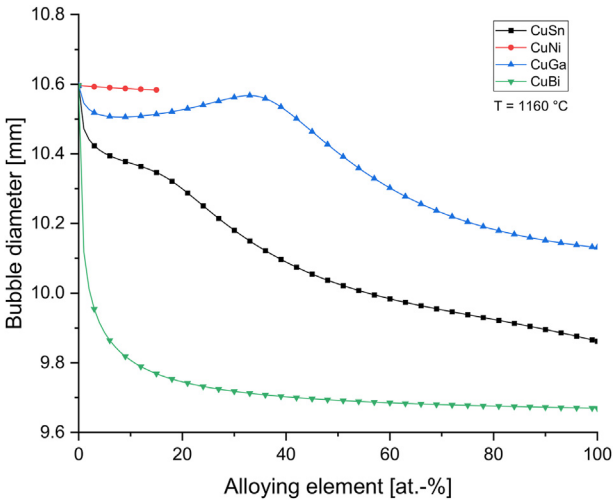

Fig. 6 – Calculated bubble diameters for the investigated melts as functions of the alloying element contents (cf. Equation (11)).

bubbles formed at single nozzles in various melts (cf. Equation (11)). The Equation is applicable at gas flow rates between 6 and 2160 ml_n/min.

$$d_b = 0.01 \cdot \left[\left(10^6 \frac{6\sigma \cdot d_{no}}{\rho_l \cdot g} \right)^2 + 0.0242 \cdot \left(10^7 \cdot Q_g \cdot d_{no}^{0.5} \right)^{1.734} \right]^{1/6} \quad (11)$$

In this Equation d_b indicates the bubble diameter, σ and ρ_l the surface tension and the density, respectively, of the melt, d_{no} the orifice outer diameter, g the gravitational acceleration, and Q_g the gas flow rate. The results of calculations performed for the investigated melts at a process temperature of 1160 °C and a gas flow rate of 500 ml_n/min are depicted in Fig. 6. The calculated bubble diameter for pure copper is 10.596 mm. An addition of bismuth leads to a sharp decrease in bubble sizes. At 100 at% Bi, a bubble diameter of 9.670 mm can be calculated which corresponds to the smallest bubbles in this work. The gradual addition of Sn leads to a steady decline in the computed diameter. For a melt of pure tin, a bubble diameter of 9.862 mm is calculated. The addition of gallium to pure liquid copper leads to a slight decrease in bubble sizes followed by an increase until a maximum bubble diameter of 10.568 mm at 33 at% Ga is reached. Further increasing the gallium content leads to a decreasing diameter to a value of 10.131 mm at 100 at% Ga. The addition of Ni to 100 at% Cu shows no significant effect in the investigated range. The calculated diameters for bubbles formed at single nozzles in the investigated alloys at 1160 °C are listed in Table 4.

Discussion

The diagrams in Fig. 3 show that for most of the investigated alloys methane conversion rates increase over experimental time. An explanation for this tendency can be found in the possible catalytic effect of solid carbon on the thermal decomposition of methane as demonstrated by Muradov, Vezirolu [45,46], and Serrano, Botas et al. [40]. With progressing experimental duration, more and more solid carbon is produced inside the melt. As this carbon is only partially carried to the hot gas filter in the gas stream and is eventually collected in the glass bottle (cf. Fig. 2), a C layer builds up that floats on the surface of the molten metal. With an increasing height of this layer, the contact time between undecomposed methane, potentially produced intermediates and solid carbon grows which enables higher reaction yields.

Equation (7) gives a superficial gas velocity of 2.5 mm/s for this work's experiments. With a column diameter of 6.5 cm, this results in a homogenous bubbly flow regime according to Shah, Kelkar et al. [30]. In this regime, the bubble sizes are mostly governed by sparger design and physical system properties as practically no coalescence or breakup occurs [28].

A comparison of calculated surface tension and bubble diameter (cf. Figures Figs. 5 and 6) with the CH_4 conversions determined in the experiments (cf. Fig. 3) gives interesting results for the investigated metals and alloys. The highest reaction yields can be reached with CuBi alloys as a medium for the pyrolysis of methane in the conducted experiments. The calculations show that these alloys have the lowest surface tension. According to Equation (11), the bubbles formed in these alloys are the smallest in comparison with the other alloys. An increase in the Bi content leads to a decrease in surface tension and bubble size. Simultaneously the reaction yield tends to improve as Bi is added to copper. This leads to the conclusion that at the process temperature of 1160 °C the improvement of the methane conversion rate primarily results from smaller bubbles, thus greater gas-liquid interfacial areas. CuSn alloys similarly follow this tendency. The addition of tin to pure copper lowers the surface tension and bubble diameter whilst also resulting in higher CH_4 conversions. The density of liquid Ga at 1160 °C is 5467.00 kg/m^3 which is significantly lower than the density of liquid copper (cf. Table 1). Therefore, an increase in the content of Ga leads to a declining surface tension but the simultaneous decrease in density of the alloy keeps the size of the formed bubbles at high values. Consequently, the utilization of CuGa alloys leads to a relatively low yield in this work. CuNi alloys are an exception to the trend stated in this section. Although the addition of Ni only insignificantly changes the relatively high values of surface tension and bubble diameter in the investigated ranges the reaction yields measured with these alloys are higher than those recorded with pure copper melts. In this case, the enhanced conversion rates can be seen as a result of the improved catalytical effect of the Ni in the alloy on the pyrolysis reaction.

As the economic feasibility of the overall process strongly depends on possible applications and marketability of the solid fraction the morphology and purity of the produced carbon are considered key parameters. Keipi, Tolvanen et al. [47] demonstrated that the properties of the pyrolysis carbon are affected by reaction temperature and catalyst. Accordingly, this work shows that the morphology of the produced carbon is highly influenced by the alloy used as a catalyst. It must be noted that for the SEM/EDS analyses the carbon is positioned on a carbon foil. Therefore, the actual metal contents may deviate from the measured values. However, the results showed that the highest number of impurities in the carbon section can be found in experiments carried out with

CuBi alloys, a consequence of the high vapor pressure of bismuth. According to Equation (5), the production of 1 kg of hydrogen results in the generation of approximately 3 kg of solid C. Therefore, possible fields of application for vast amounts of pyrolysis carbon must be determined assuming a potential transition of the global hydrogen production to methane pyrolysis. These may include a substitution of cement for the manufacture of concrete or an introduction into the soil to improve its quality. Especially pursuing the latter makes considerations of statutory thresholds of the respective metals mandatory with a view to process adaptions if necessary.

Conclusions

A transition of the energy system from fossil to renewable sources is mandatory to sustain human prosperity in the 21st century. Research and development of processes for the production and utilization of hydrogen to substitute conventional energy carriers and reducing agents, especially in important industrial sectors will play key roles on the way to a clean and secure future.

In this work, hydrogen and solid carbon were produced by the thermo-catalytical decomposition of methane in a molten metal reactor with a height of the melt of 7 cm using different molten copper alloys and metals, respectively. Methane was introduced into the melt utilizing an alumina lance at 500 ml_n/min. The effects of adding bismuth, nickel, tin, or gallium to pure copper were investigated by measuring the amount of produced hydrogen and subsequently calculating the according methane conversion rates. CuBi showed the best effectivity as a medium in methane pyrolysis at 1160 °C, followed by CuNi, CuSn, and CuGa. The highest methane conversion rate of 68.44% could be recorded with CuBi80. Calculations showed that the addition of Bi, Sn, or Ga impacts the surface tension of the melt and the size of the bubbles which are formed at the lance. A comparison of the calculated results with the experimental CH_4 conversion rates demonstrated a strong influence of surface tension and bubble size, thus a bigger gas-liquid interfacial area on the reaction yields. The addition of Ni to Cu results in negligible changes in surface tension and bubble diameter. This observation leads to the conclusion that the effect of a relatively small interfacial area is in this case counterbalanced by the high catalytic effectiveness of CuNi alloys. Furthermore, the effect of a growing layer of carbon that floats on the melt was measured. With progressing experimental duration most of the experiments resulted in higher conversion rates. The described phenomena require further investigation.

The produced carbon was investigated by SEM/EDS and BSE analyses. The results demonstrate that properties of the pyrolysis carbon, especially morphology, can be influenced using different alloys. The purity of the carbon section must be taken into consideration given possible areas of application.

The results of the conducted experiments show that the products of methane pyrolysis can be strongly influenced by a change in the used catalyst. For the achievement of economic competitivity in comparison with other hydrogen production processes, especially steam reforming of methane, further investigation of the process parameters and their influence on the reaction kinetics and product purity is of crucial importance [48].

Declaration of competing interest

The authors declare that they have no known competing financial interests or personal relationships that could have appeared to influence the work reported in this paper.

REFERENCES

[1] Pegels A, Altenburg T. Latecomer development in a "greening" world: introduction to the special issue, vol. 135. World Development; 2020, 105084. https://doi.org/10.1016/j.worlddev.2020.105084.

[2] IEA. World energy outlook 2021. Paris: IEA; 2021.

[3] J. Tian, L. Yu, R. Xue, S. Zhuang and Y. Shan, Global low-carbon energy transition in the post-COVID-19 era. Appl Energy 307 (2022), pp. 118205. doi:10.1016/j.apenergy.2021.118205

[4] Caglayan DG, Heinrichs HU, Robinius M, Stolten D. Robust design of a future 100% renewable european energy supply system with hydrogen infrastructure. Int J Hydrogen Energy 2021;46(57):29376–90. https://doi.org/10.1016/j.ijhydene.2020.12.197.

[5] Olabi AG, bahri As, Abdelghafar AA, Baroutaji A, Sayed ET, Alami AH, Rezk H, Abdelkareem MA. Large-vscale hydrogen production and storage technologies: current status and future directions. Int J Hydrogen Energy 2021;46(45):23498–528. https://doi.org/10.1016/j.ijhydene.2020.10.110.

[6] Kovač A, Paranos M, Marciuš D. Hydrogen in energy transition: a review. Int J Hydrogen Energy 2021;46(16):10016–35. https://doi.org/10.1016/j.ijhydene.2020.11.256.

[7] Acar C, Dincer I. Review and evaluation of hydrogen production options for better environment. J Clean Prod 2019;218:835–49. https://doi.org/10.1016/j.jclepro.2019.02.046.

[8] IEA, Global. Hydrogen review 2021. Paris: IEA; 2021.

[9] Chai S, Zhang G, Li G, Zhang Y. Industrial hydrogen production technology and development status in China: a review. Clean Technol Environ Policy 2021;23(7):1931–46. https://doi.org/10.1007/s10098-021-02089-w.

[10] Kothari R, Buddhi D, Sawhney RL. Comparison of environmental and economic aspects of various hydrogen production methods. Renew Sustain Energy Rev 2008;12(2):553–63. https://doi.org/10.1016/j.rser.2006.07.012.

[11] Song C, Liu Q, Ji N, Kansha Y, Tsutsumi A. Optimization of steam methane reforming coupled with pressure swing adsorption hydrogen production process by heat integration. Appl Energy 2015;154:392–401. https://doi.org/10.1016/j.apenergy.2015.05.038.

[12] Parkinson B, Tabatabaei M, Upham DC, Ballinger B, Greig C, Smart S, McFarland E. Hydrogen production using methane: techno-economics of decarbonizing fuels and chemicals. Int J Hydrogen Energy 2018;43(5):2540–55. https://doi.org/10.1016/j.ijhydene.2017.12.081.

[13] Machhammer O, Bode A, Hormuth W. Financial and ecological evaluation of hydrogen production processes on large scale. Chem Eng Technol 2016;39(6):1185–93. https://doi.org/10.1002/ceat.201600023.

[14] Singh Aulakh DJ, Boulama KG, Pharoah JG. On the reduction of electric energy consumption in electrolysis: a thermodynamic study. Int J Hydrogen Energy 2021;46(33):17084–96. https://doi.org/10.1016/j.ijhydene.2021.02.161.
[15] Ebner T, Sprung A, Hochfellner A, Samberger S, Antrekowitsch H. Preliminary investigations on Methane Pyrolysis for the Production of H2 in a Molten Metal Bath Voruntersuchungen zur Methanpyrolyse zur Herstellung von H2 im flüssigen Metallbad. World of Metallurgy – ERZMETALL 2021;74(2):84–9.
[16] Diab J, Fulcheri L, Hessel V, Rohani V, Frenklach M. Why turquoise hydrogen will Be a game changer for the energy transition. Int J Hydrogen Energy 2022. https://doi.org/10.1016/j.ijhydene.2022.05.299.
[17] Riley J, Atallah C, Siriwardane R, Stevens R. Technoeconomic analysis for hydrogen and carbon Co-Production via catalytic pyrolysis of methane. Int J Hydrogen Energy 2021;46(39):20338–58. https://doi.org/10.1016/j.ijhydene.2021.03.151.
[18] Serban M, Lewis MA, Marshall CL, Doctor RD. Hydrogen production by direct contact pyrolysis of natural gas. Energy Fuels 2003;17(3):705–13. https://doi.org/10.1021/ef020271q.
[19] Plevan M, Geißler T, Abánades A, Mehravaran K, Rathnam RK, Rubbia C, Salmieri D, Stoppel L, Stückrad S, Wetzel T. Thermal cracking of methane in a liquid metal bubble column reactor: experiments and kinetic analysis. Int J Hydrogen Energy 2015;40(25):8020–33. https://doi.org/10.1016/j.ijhydene.2015.04.062.
[20] Geißler T, Abánades A, Heinzel A, Mehravaran K, Müller G, Rathnam RK, Rubbia C, Salmieri D, Stoppel L, Stückrad S, Weisenburger A, Wenninger H, Wetzel T. Hydrogen production via methane pyrolysis in a liquid metal bubble column reactor with a packed bed. Chem Eng J 2016;299:192–200. https://doi.org/10.1016/j.cej.2016.04.066.
[21] Upham DC, Agarwal V, Khechfe A, Snodgrass ZR, Gordon MJ, Metiu H, McFarland EW. Catalytic molten metals for the direct conversion of methane to hydrogen and separable carbon. Science (New York, NY) 2017;358(6365):917–21. https://doi.org/10.1126/science.aao5023.
[22] Rahimi N, Kang D, Gelinas J, Menon A, Gordon MJ, Metiu H, McFarland EW. Solid carbon production and recovery from high temperature methane pyrolysis in bubble columns containing molten metals and molten salts. Carbon 2019;151:181–91. https://doi.org/10.1016/j.carbon.2019.05.041.
[23] Palmer C, Tarazkar M, Kristoffersen HH, Gelinas J, Gordon MJ, McFarland EW, Metiu H. Methane pyrolysis with a molten Cu–Bi alloy catalyst. ACS Catal 2019;9(9):8337–45. https://doi.org/10.1021/acscatal.9b01833.
[24] Zeng J, Tarazkar M, Pennebaker T, Gordon MJ, Metiu H, McFarland EW. Catalytic methane pyrolysis with liquid and vapor phase tellurium. ACS Catal 2020;10(15):8223–30. https://doi.org/10.1021/acscatal.0c00805.
[25] Leal Pérez BJ, Medrano Jiménez JA, Bhardwaj R, Goetheer E, van Sint Annaland M, Gallucci F. Methane pyrolysis in a molten gallium bubble column reactor for sustainable hydrogen production: proof of concept & techno-economic assessment. Int J Hydrogen Energy 2021;46(7):4917–35. https://doi.org/10.1016/j.ijhydene.2020.11.079.
[26] Zaghloul N, Kodama S, Sekiguchi H. Hydrogen production by methane pyrolysis in a molten-metal bubble column. Chem Eng Technol 2021;44(11):1986. https://doi.org/10.1002/ceat.202100210.
[27] Degaleesan S, Dudukovic M, Pan Y. Experimental study of gas-induced liquid-flow structures in bubble columns. AIChE J 2001;47(9):1913–31. https://doi.org/10.1002/aic.690470904.
[28] Thorat BN, Joshi JB. Regime transition in bubble columns: experimental and predictions. Exp Therm Fluid Sci 2004;28(5):423–30. https://doi.org/10.1016/j.expthermflusci.2003.06.002.
[29] Hyndman CL, Larachi F, Guy C. Understanding gas-phase hydrodynamics in bubble columns: a convective model based on kinetic theory. Chem Eng Sci 1997;52(1):63–77. https://doi.org/10.1016/S0009-2509(96)00387-9.
[30] Shah YT, Kelkar BG, Godbole SP, Deckwer W-D. Design parameters estimations for bubble column reactors. AIChE J 1982;28(3):353–79. https://doi.org/10.1002/aic.690280302.
[31] Kováts P, Thévenin D, Zähringer K. Characterizing fluid dynamics in a bubble column aimed for the determination of reactive mass transfer. Heat Mass Tran 2018;54(2):453–61. https://doi.org/10.1007/s00231-017-2142-0.
[32] Daly JG, Patel SA, Bukur DB. Measurement of gas holdups and sauter mean bubble diameters in bubble column reactors by dynamics gas disengagement method. Chem Eng Sci 1992;47(13–14):3647–54. https://doi.org/10.1016/0009-2509(92)85081-L.
[33] Zahedi P, Saleh R, Moreno-Atanasio R, Yousefi K. Influence of fluid properties on bubble formation, detachment, rising and collapse; Investigation using volume of fluid method. Kor J Chem Eng 2014;31(8):1349–61. https://doi.org/10.1007/s11814-014-0063-x.
[34] Tate T. On the magnitude of a drop of liquid formed under different circumstances. The London, Edinburgh, and Dublin Philosophical Magazine and Journal of Science 1864;27(181):176–80. https://doi.org/10.1080/14786446408643645.
[35] Mori K, Sano M, Sato T. Size of bubbles formed at single nozzle immersed in molten iron. ISIJ Int 1979;19(9):553–8. https://doi.org/10.2355/isijinternational1966.19.553.
[36] Sano M, Mori K. Size of bubbles in energetic gas injection into liquid metal. ISIJ Int 1980;20(10):675–81. https://doi.org/10.2355/isijinternational1966.20.675.
[37] Smithells metals reference book. 8th ed. Amsterdam, Boston: Elsevier Butterworth-Heinemann; 2004.
[38] Butler JAV. The thermodynamics of the surfaces of solutions. Proc Roy Soc Lond A 1932;135(827):348–75. https://doi.org/10.1098/rspa.1932.0040.
[39] an Mey S. Thermodynamic re-evaluation of the Cu-Ni system. Calphad 1992;16(3):255–60. https://doi.org/10.1016/0364-5916(92)90022-P.
[40] Niemelä J, Effenberg G, Hack K, Spencer PJ. A thermodynamic evaluation of the copper — bismuth and copper — lead systems. Calphad 1986;10(1):77–89. https://doi.org/10.1016/0364-5916(86)90011-8.
[41] Li D, Franke P, Fürtauer S, Cupid D, Flandorfer H. The Cu–Sn phase diagram part II: new thermodynamic assessment. Intermetallics 2013;34:148–58. https://doi.org/10.1016/j.intermet.2012.10.010.
[42] Li J-B, Ji LN, Liang JK, Zhang Y, Luo J, Li CR, Rao GH. A thermodynamic assessment of the copper–gallium system. Calphad 2008;32(2):447–53. https://doi.org/10.1016/j.calphad.2008.03.006.
[43] Speiser R, Poirier DR, Yeum K. Surface tension of binary liquid alloys. Scripta Metall 1987;21(5):687–92. https://doi.org/10.1016/0036-9748(87)90385-1.
[44] Tanaka T, Hack K, Iida T, Hara S. Application of thermodynamic databases to the evaluation of surface tensions of molten alloys, salt mixtures and oxide mixtures. Int J Mater Res 1996;87(5):380–9. https://doi.org/10.1515/ijmr-1996-870509.
[45] Muradov N, Vezirolu T. From hydrocarbon to hydrogen? carbon to hydrogen economy. Int J Hydrogen Energy 2005;30(3):225–37. https://doi.org/10.1016/j.ijhydene.2004.03.033.

[46] Serrano DP, Botas JA, Guil-Lopez R. H2 production from methane pyrolysis over commercial carbon catalysts: kinetic and deactivation study. Int J Hydrogen Energy 2009;34(10):4488–94. https://doi.org/10.1016/j.ijhydene.2008.07.079.
[47] Keipi T, Tolvanen KE, Tolvanen H, Konttinen J. Thermo-catalytic decomposition of methane: the effect of reaction parameters on process design and the utilization possibilities of the produced carbon. Energy Convers Manag 2016;126:923–34. https://doi.org/10.1016/j.enconman.2016.08.060.
[48] Jäger H, Frohs W. Industrial carbon and graphite materials: raw materials, production and applications. Weinheim, Germany: Wiley-VCH; 2021.